

## Design of DAS fibres for elastic wave mode discrimination

Kris Innanen and Matthew Eaid

### ABSTRACT

In 2016 a “Fibre Geometry and Sensing Model” was introduced in order to facilitate characterization of DAS fibres and their shapes as they respond to various types of elastic wave. The directionality of an arbitrary fibre and its capacity to enable multicomponent DAS sensing were both considered. The model grew considerably in 2017 and now contains the beginnings of a framework to analyze the characteristic response of a given fibre shape to a range of different elastic modes, P- and S-waves at a range of 3D obliquities, and Rayleigh waves for instance. The model can be set up to experience these waves in a useful form, “lighting up” in regions where the fibre response is above a given threshold. These responses are planned to be the basis for designing fibres which can optimally enhance certain wave modes (e.g., body waves) and suppress others (e.g., surface waves).

### INTRODUCTION

Distributed Acoustic Sensing (DAS) with fibre-optic technology is emerging as a potentially powerful and inexpensive form of seismic acquisition (e.g., Daley et al., 2013). Hardware (fibre-optics and interrogator) systems are increasing the signal-to-noise ratio of DAS data and its resolution, and algorithms for passive seismic sensing (Ajo-Franklin et al., 2015) as well as acquisition, processing, and interpretation regimens for active-source reflection and VSP data (Mateeva et al., 2012, 2013, 2014; Chalenski et al., 2016) are undergoing fairly rigorous validation and review as of late 2017.

The sensitivity of a fibre-optic interval to axial strain, i.e., longitudinal strain in the direction of the axis of the fibre, and its insensitivity to other strain components, is the root of one of the main weaknesses of DAS systems, its so-called *broadside insensitivity* (Mateeva et al., 2014; Kuvshinov, 2016). To enrich the broadside DAS signal, shaped fibres have been introduced, notably the helical-wound cable (HWC), in which a fibre strand is wrapped in a helix about a roughly 1cm mandrel and jacketed. At the Containment and Monitoring Institute Field Research Station (CaMI-FRS), horizontal trenched fibre and vertical fibre attached to well-casing, in both straight and HWC configurations, have been deployed alongside standard 3C geophones (Lawton, 2017).

With the introduction of shaped fibres several important questions appear. Firstly, although qualitatively there is an expectation of an increased broadside sensitivity, what quantitatively are the sensitivities for a given shape? This critical issue is affected by channel spacing, gauge length, elastic wave mode impinging on the fibre, amongst others. Secondly, if the axial strains from a range of directions are now being sensed, by virtue of the new fibre tangent directions produced by the helical wrapping, do opportunities for multicomponent sensing exist (Ning and Sava, 2016; Innanen, 2017)? Thirdly, assuming that HWC has limitations, both in terms of increasing broadside sensitivity, and supporting multicomponent sensing, are there practical shape alterations that will act as enablers for these two needs? These questions were the main focus of last year’s report (Innanen, 2016).

In this paper a fourth question is addressed. In standard (geophone based) acquisition the geophone itself is the elementary sensor, but a range of high-level acquisition goals can be addressed through design of geophone arrays (e.g., Anstey, 1986)—or at least so it was in the past—and/or deployment of dense acquisition modes, followed by stacking, averaging or some more complex procedure. Stacking signal over horizontal arrays, for instance, will tend to suppress waves propagating horizontally and enhance waves propagating vertically. Question: in seismic acquisition based not on geophones but on DAS fibre, what does the equivalent of *array design* and/or signal enhancing/suppressing of dense acquisition design look like?

We might, for instance, wish to design a fibre such that one set of elastic wave modes, e.g., P- and S-waves, is enhanced, while another, e.g., Rayleigh waves, is suppressed in its response. Or, one for which P- and S-wave modes are both maintained, but are discriminated. Or, finally, in which up-going P- and S-waves are discriminated from down-going modes. Are such things possible?

To answer this question the response of a candidate fibre, with its shape, gauge length, channel spacing, SNR, etc., to incident wave modes of all these types must be understood. Once response patterns to desirable and undesirable modes are known, optimum shapes which (through stacking or selective suppression of signal patterns) enhance the former or suppress the latter can be sought.

The fibre model, which we will refer to as the *CREWES fibre geometry and sensing model*, or FGSM, is well-placed to act as a starting point for this endeavour. In this paper we describe the formulation and behaviour of the forward model by which shape design criteria can be analyzed. The focus is on the response of various shapes and acquisition parameters to active source acquisition, and simple P-, S-, and Rayleigh waveforms and their influence on fibres of various types. In one companion paper the FGSM is coupled to a full 3D elastic finite difference model to simulate a realistic field response (Eaid and Innanen, 2017); in another the potential for shaped DAS fibres to characterize the source characteristics of microseismic events is developed (Innanen and Mahmoudian, 2017).

## **THE CREWES FIBRE GEOMETRY AND SENSING MODEL (FGSM)**

A model capturing the effect of fibre geometry on response to elastic wave modes was introduced last year (Innanen, 2016), motivated initially by a need to characterize the response of straight versus helical-wound cable (HWC) and an interest in appraising the 6C sensing problem. Its development since then is represented in Figure 1. A set of functions (green boxes) allow fibre / interrogator details (gauge length, channel spacing, helix radius, lead angle, etc.) to be incorporated while the key features of the fibre are computed (primarily tangent directions and arc-lengths). These can be coupled with input snapshots of elastic wave strains to model a general response within a DAS system (Eaid and Innanen, 2017).

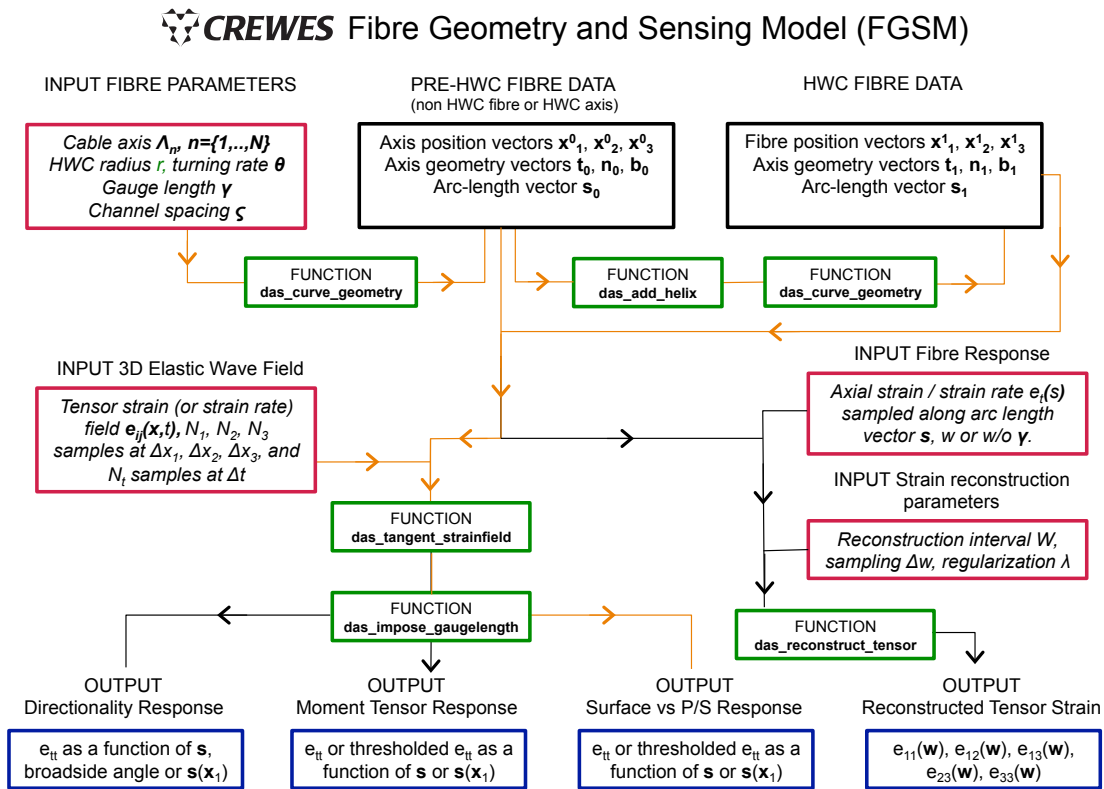


FIG. 1. Current status of the gradually accreting fibre geometry and sensing model. Inputs for the various applications of the model are in red boxes; the key functions operating within the model are in green boxes; the current applications of the model are in blue boxes.

### Straight, helical, and 2-helical benchmarking fibres

Straight and helical-wound fibre shapes are already commercially available and are in place in both horizontal-trenched and vertical-borehole configurations at the CaMI-FRS, where CREWES is and will be carrying out extensive field work (Lawton, 2017). We create two benchmark numerical models of such fibres with the FGSM model based on these, with the latter undergoing one turn every 10cm. To add a third, more complex shape to this benchmark set, we incorporate a 2-helix matching what would be derived if the HWC was wound about a 50cm diameter well-casing at a rate of one full turn every 3m. These fibres are illustrated in Figure 2; note, the HWC radius is exaggerated to 3cm for illustration purposes.

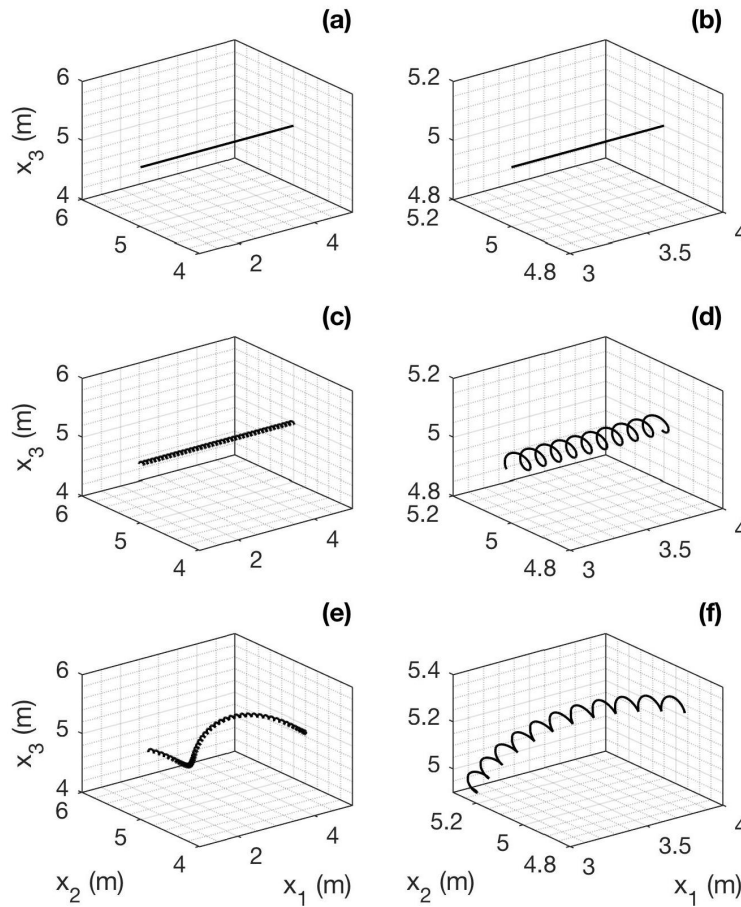


FIG. 2. Sections of three benchmark fibre designs for analysis of the elastic wave mode discrimination problem are illustrated at two different zoom-levels. (a)-(b) straight fibre viewed at two scales; (c)-(d) HWC; (e)-(f) 2-helix.

### BODY- AND SURFACE-WAVE ELASTIC STRAIN

The results of this paper arise from a coupling between the FGSM and some simple models of the strain or strain rate carried by various key elastic modes. In this section we develop useful expressions for the strains experienced within the same volumes occupied by the benchmark DAS fibres assembled in the previous section.

## Body-wave strains

We begin the process of characterizing the fibre response to various incident wave modes, by parameterizing the strains carried by elastic body and surface waves impinging on the fibre from various directions. Here we consider “static” cases, in which we idealize the sensing by illuminating the entire fibre with a constant strain tensor corresponding to P- or S-waves. This can be used to quantify the instantaneous response of a segment of fibre within the dominant wavelength of an impinging wave.

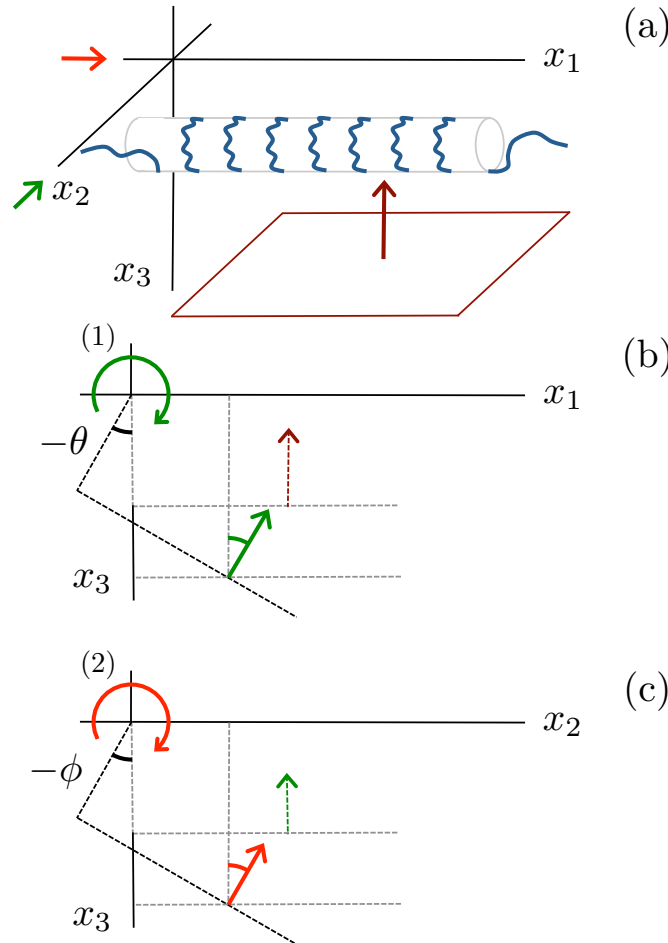


FIG. 3. Obliquely incident body waves. (a) Plane body wave incident along the  $-x_3$  direction. “Look” directions for rotations (1) and (2) are indicated in green and red respectively. (b) Rotation (1) is counterclockwise by  $\theta$  degrees about the  $x_2$  axis. (c) Rotation (2) is counterclockwise by  $\phi$  degrees about the  $x_1$  axis. For drawing convenience, clockwise rotations  $-\theta$  and  $-\phi$  are illustrated.

### *Normally-incident plane P- and S-waves (static case)*

The static case is treated first. We begin by considering plane P- and S-waves incident on the benchmark fibres normally and from directly below, i.e., in the  $-x_3$  direction. When a P-wave with these properties passes through the volume containing the fibre, at a fixed instant and within the dominant wavelength, it will impose an approximately constant strain

on the medium of the form

$$\mathbf{e}_P = \begin{bmatrix} 0 & 0 & 0 \\ 0 & 0 & 0 \\ 0 & 0 & e_P \end{bmatrix}. \quad (1)$$

The strain rate will have the same form but with  $e_P$  replaced by  $\dot{e}_P$ ; from here onward we will proceed assuming the fibre is sensitive to raw strain; as all of our considerations are based on spatial variations, no significant changes to the results will occur if this is replaced with strain-rate. When an S-wave with arbitrary polarization is incident, the strain is instead

$$\mathbf{e}_S = \begin{bmatrix} 0 & 0 & e_S \\ 0 & 0 & e'_S \\ e_S & e'_S & 0 \end{bmatrix}. \quad (2)$$

### *Obliquely-incident plane P- and S-waves (static case)*

Any fibre design which works to realistically accentuate such body waves will need to consider their response over a range of incidence angles. To accommodate this, we next allow the previously-designed incident wave vectors carrying these P- and S-wave strains to be rotated arbitrarily. In Figure 3, the field coordinate system is illustrated:  $x_1$  acts as a principle, or inline axis,  $x_2$  acts as a crossline axis, and  $x_3$  represents depth. The two pure rotations employed to generalize the P- and S-waves, involving a “polar” angle  $\theta$  about the  $x_2$  axis and an “azimuthal” angle  $\phi$  about the  $x_1$  axis, are illustrated in Figures 3b-c.

If a basic, vertically-incident strain tensor  $\mathbf{e}_P$  or  $\mathbf{e}_S$  is given, along with a desired incidence direction characterized by the pair  $(\theta, \phi)$ , the fibre is then exposed to a strain of

$$\mathbf{e}_P(\theta, \phi) = \mathbf{R}(\theta, \phi) \begin{bmatrix} 0 & 0 & 0 \\ 0 & 0 & 0 \\ 0 & 0 & e_P \end{bmatrix} \mathbf{R}^T(\theta, \phi), \quad (3)$$

or

$$\mathbf{e}_S(\theta, \phi) = \mathbf{R}(\theta, \phi) \begin{bmatrix} 0 & 0 & e_S \\ 0 & 0 & e'_S \\ e_S & e'_S & 0 \end{bmatrix} \mathbf{R}^T(\theta, \phi), \quad (4)$$

where the rotation through first  $\theta$  then  $\phi$  is enacted by

$$\mathbf{R}(\theta, \phi) = \begin{bmatrix} \cos \phi & -\cos \theta \sin \phi & \sin \theta \sin \phi \\ \sin \phi & \cos \theta \cos \phi & -\sin \theta \cos \phi \\ 0 & \sin \theta & \cos \theta \end{bmatrix}. \quad (5)$$

### *Obliquely-incident harmonic plane P-waves (dynamic case)*

We also consider “dynamic” cases, in which idealized time-varying P-waves impinge on the three benchmark fibres. We will here focus on plane harmonic P-waves incident at

an angle  $\theta$  measured from the vertical axis and oblique to the inline  $x_1$  axis (i.e., the angle is generated by rotating a vertical wave vector about the  $x_2$  axis). Choosing a cosine wave and having it propagate at a velocity of  $V_P$ , the displacement associated with such a wave is

$$\mathbf{u}(\mathbf{x}, t) = \begin{bmatrix} u_1(x_1, x_3, t) \\ u_3(x_1, x_3, t) \end{bmatrix}, \quad (6)$$

where

$$\begin{aligned} u_1(x_1, x_3, t) &= -\sin \theta \cos k(x_3 - V_P t) \\ u_3(x_1, x_3, t) &= \cos \theta \cos k(x_3 - V_P t). \end{aligned} \quad (7)$$

Using the rule

$$e_{ij} = \frac{1}{2} (\partial_j u_i + \partial_i u_j), \quad (8)$$

this implies a space and time varying strain tensor

$$\mathbf{e} = \begin{bmatrix} e_{11} & e_{12} & e_{13} \\ & e_{22} & e_{23} \\ & & e_{33} \end{bmatrix}, \quad (9)$$

where

$$\begin{aligned} e_{13} &= \left( \frac{k \sin \theta}{2} \right) \sin k(x_3 - V_P t), \\ e_{33} &= -\left( \frac{k \cos \theta}{2} \right) \sin k(x_3 - V_P t), \quad \text{and} \\ e_{11} &= e_{12} = e_{22} = e_{23} = 0. \end{aligned} \quad (10)$$

## Surface wave strain

### *Plane harmonic Rayleigh waves propagating in the $x_1$ direction*

A little bit of development is necessary to determine the strain response of a Rayleigh wave (ground roll) mode. We will consider a simple plane harmonic Rayleigh wave propagating along the inline ( $x_1$ ) direction mimicking the ground roll response of a 2D experiment carried out above a trenched fibre. Let the displacement of such a wave be the vector  $\mathbf{u}$ , i.e.,

$$\mathbf{u}(\mathbf{x}, t) = \begin{bmatrix} u_1(x_1, x_2, x_3, t) \\ u_2(x_1, x_2, x_3, t) \\ u_3(x_1, x_2, x_3, t) \end{bmatrix}, \quad (11)$$

such that if the particle motion is confined to the 1-3 plane it reduces as with the dynamic P-wave to

$$\mathbf{u}(\mathbf{x}, t) = \begin{bmatrix} u_1(x_1, x_3, t) \\ u_3(x_1, x_3, t) \end{bmatrix}. \quad (12)$$

In a homogeneous isotropic-elastic halfspace, the plane harmonic Rayleigh wave is non-dispersive with displacement components given by (e.g., Ewing et al., 1957)

$$\begin{aligned} u_1(x_1, x_3, t) &= c_1 (c_2 e^{c_3 k x_3} + c_4 e^{c_5 k x_3}) \cos k (x_1 - v_R t) \\ u_3(x_1, x_3, t) &= c_1 (c_3 e^{c_3 k x_3} + c_6 e^{c_5 k x_3}) \sin k (x_1 - v_R t), \end{aligned} \quad (13)$$

where  $v_R = 0.9194\beta$ . An example set of constants  $c_1$ - $c_6$  is given in Table 1. So, again using the rule

$$e_{ij} = \frac{1}{2} (\partial_j u_i + \partial_i u_j), \quad (14)$$

the strain tensor carried by this wave at every point in space is

$$\mathbf{e} = \begin{bmatrix} e_{11} & e_{12} & e_{13} \\ & e_{22} & e_{23} \\ & & e_{33} \end{bmatrix}, \quad (15)$$

where

$$\begin{aligned} e_{11} &= \lambda_1 k (\lambda_2 e^{\lambda_3 k x_3} + \lambda_4 e^{\lambda_5 k x_3}) \sin k (x_1 - v_R t), \\ e_{13} &= \lambda_6 k [\lambda_7 e^{\lambda_3 k x_3} + \lambda_8 e^{\lambda_5 k x_3}] \cos k (x_1 - v_R t), \\ e_{33} &= \lambda_9 k (\lambda_{10} e^{\lambda_3 k x_3} + \lambda_{11} e^{\lambda_5 k x_3}) \sin k (x_1 - v_R t), \quad \text{and} \\ e_{12} &= e_{22} = e_{23} = 0. \end{aligned} \quad (16)$$

The coefficients  $\lambda_1$ - $\lambda_{11}$  are given in Table 2.

Constant	Value
$c_1$	1.0000
$c_2$	1.0000
$c_3$	-0.8475
$c_4$	-0.5773
$c_5$	-0.3933
$c_6$	1.4679

Table 1. Displacement coefficients for the plane harmonic Rayleigh wave.

## MODELING THE ACTIVATION OF SHAPED DAS FIBRES BY BODY AND SURFACE WAVES

The next step is to couple these static and dynamic elastic wave motions with the CREWES-FGSM. The model is in its current form already configured to accept a 3D discretized volume of tensor strain elements, and then project them onto any desired fibre embedded in a (mathematical) volume with the same dimensions. Beyond this, a threshold is set as the criterion for whether the strain as sensed by a fibre, with or without an imposed gauge length, is significant or not. Our initial examination of it will be largely visual. It involves plots of the DAS fibres, along which arc-length intervals with responses exceeding the threshold are “lit up”, giving a sense of the strength and character of the signal.

Constant	Value
$\lambda_1$	$-c_1$
$\lambda_2$	$c_2$
$\lambda_3$	$c_3$
$\lambda_4$	$c_4$
$\lambda_5$	$c_5$
$\lambda_6$	$c_1/2$
$\lambda_7$	$c_3(1 + c_2)$
$\lambda_8$	$c_6 + c_4c_5$
$\lambda_9$	$c_1$
$\lambda_{10}$	$c_3^2$
$\lambda_{11}$	$c_5c_6$

Table 2. Strain coefficients for the plane harmonic Rayleigh wave.

### P- and S-wave activation of shaped DAS fibres (static)

The static P- and S-wave strains can be investigated (and ultimately averaged or in some way summarized) over meaningful ranges of angles of obliquity. In these sections we will show some examples of this happening.

In Figure 4 a helical-wound cable (HWC) fibre configuration is adopted and illuminated with a P-wave over a range of angles. Intervals of the fibre whose response exceeds the threshold are coloured red. The HWC turning rate has been exaggerated for illustration purposes.

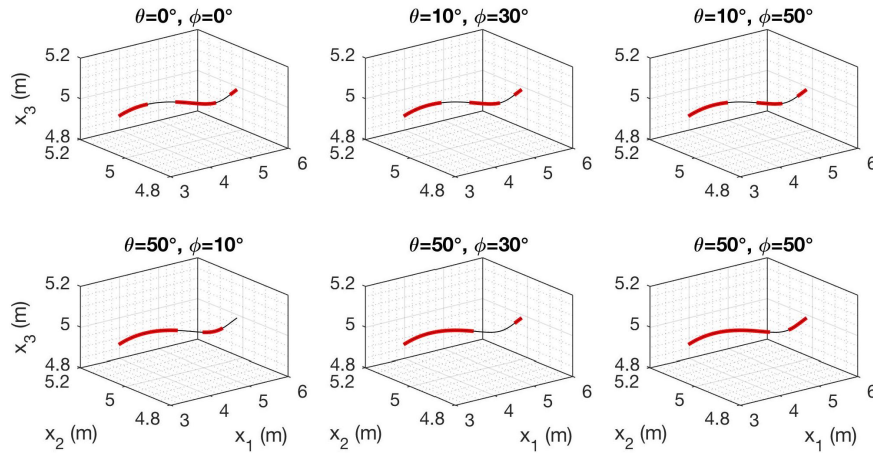


FIG. 4. Response of a HWC system to vertically-propagating P-wave with oblique incidence;  $\theta$  is the angle about the  $x_2$  axis and  $\phi$  the angle about the  $x_1$  axis. Fibre elements whose turn brings them broadside to the incident wave are insensitive.

In Figure 5 the same helical-wound cable (HWC) fibre configuration is illuminated with a vertically-propagating S-wave with displacement  $45^\circ$  to the  $x_1$ - $x_2$  axes, subsequently rotated through a range of angles. Intervals of the fibre whose response exceeds the threshold are coloured red. The HWC turning rate has been exaggerated for illustration purposes.

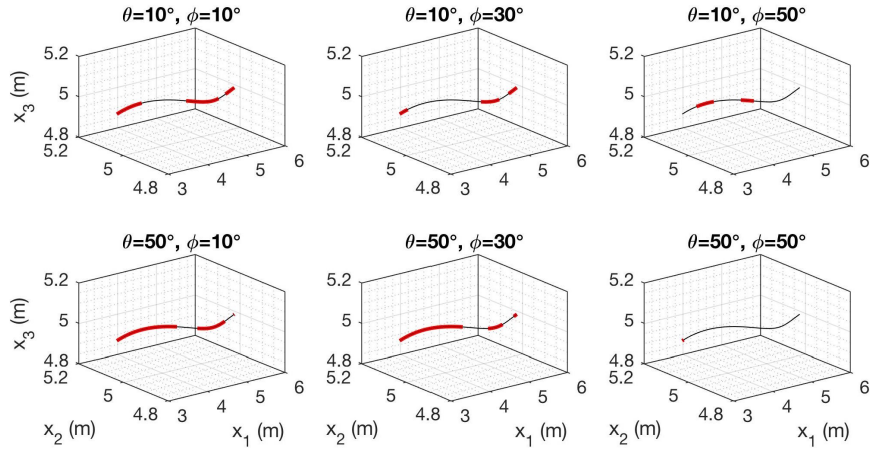


FIG. 5. Response of a HWC system to vertically-propagating S-wave with oblique incidence;  $\theta$  is the angle about the  $x_2$  axis and  $\phi$  the angle about the  $x_1$  axis.

In Figures 6-7 the benchmark 2-helix fibres are “bathed” in the same elastic strains as the HWC fibres in Figures 4 and 5.

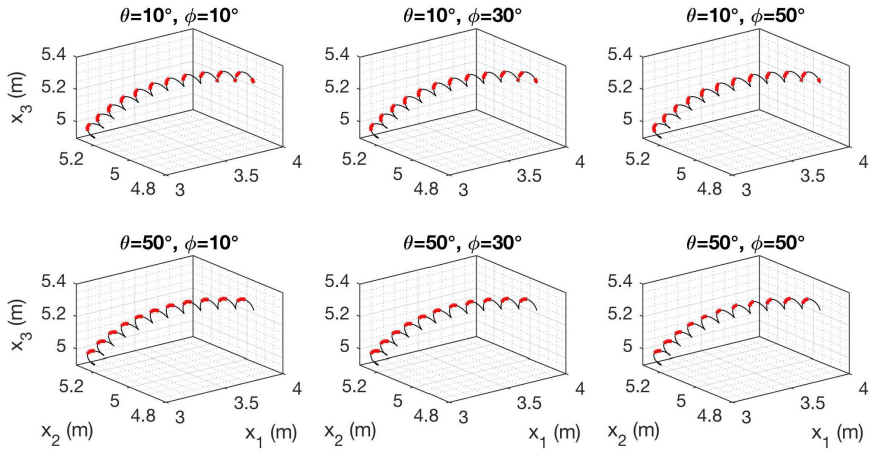


FIG. 6. Response of a 2-helix system to vertically-propagating P-wave with oblique incidence;  $\theta$  is the angle about the  $x_2$  axis and  $\phi$  the angle about the  $x_1$  axis. Fibre elements whose turn brings them broadside to the incident wave are insensitive.

These figures give the essential picture of the response thresholding procedure. We note that the 2-helix responds to obliquely incident elastic strains with significantly increased complexity in comparison to the HWC.

**P-wave activation of shaped DAS fibres (dynamic)**

The dynamic activation of a DAS fibre is a more complete way of understanding how body versus surface wave modes affect a fibre. In Figures 8–11 the response to a dynamic P-wave with fixed obliquity (rotated about the  $x_2$  axis) is illustrated at instants during its propagation.

In each figure, the left panel is a plot of the shape of the fibre and its position in the

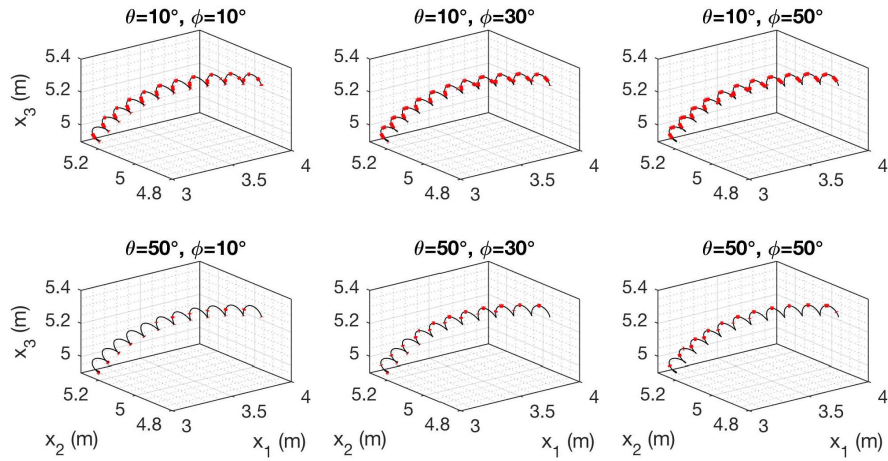


FIG. 7. Response of a 2-helix system to vertically-propagating S-wave with oblique incidence;  $\theta$  is the angle about the  $x_2$  axis and  $\phi$  the angle about the  $x_1$  axis.

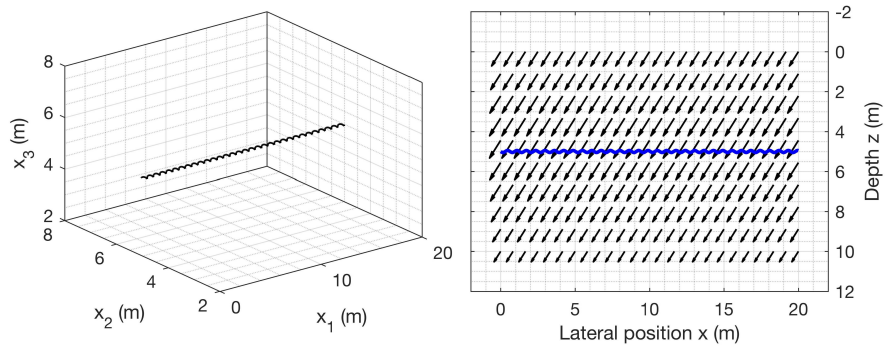


FIG. 8. Response of the benchmark HWC fibre (left panel) to a dynamic, plane-harmonic P-wave at oblique incidence (right panel). The displacement field at a given instant is plotted in the right panel, overlain by the projection of the fibre into the  $x_1$ - $x_3$  plane (blue). Intervals of the fibre in the right panel whose response exceeds a certain threshold are coloured red.

volume being illuminated (black). In the right panel the P-wave displacement field at the instant of illumination is plotted in the vicinity of the fibre (the plot is a profile in the  $x_1$ - $x_3$  plane; in these examples all wavefields are held constant in the  $x_2$  direction). In the FGSM, the displacement field is transformed into a tensor strain field, and projected onto the current fibre (illustrated in the right panel in blue). Intervals of the fibre (as illustrated in the left panels) for which the response exceeds a chosen threshold are coloured red.

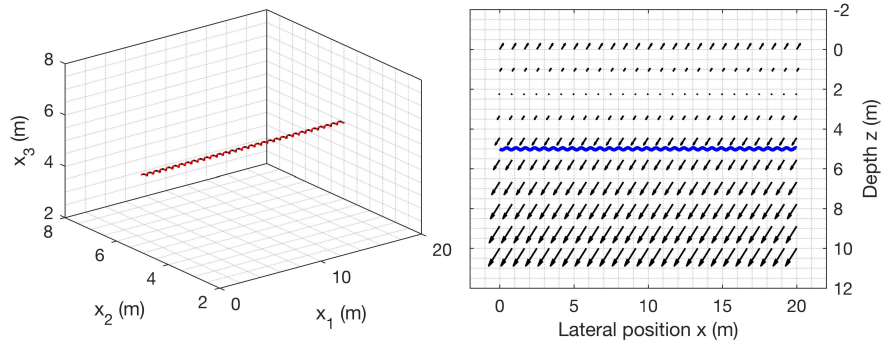


FIG. 9. Response of the benchmark HWC fibre (left panel) to a dynamic, plane-harmonic P-wave at oblique incidence (right panel). The displacement field at a given instant is plotted in the right panel, overlain by the projection of the fibre into the  $x_1$ - $x_3$  plane (blue). Intervals of the fibre in the right panel whose response exceeds a certain threshold are coloured red. This plot corresponds to the instant of time subsequent to that in Figure 8.

This configuration is plotted four times. In Figures 8-9 the P-wave at two consecutive instants as projected onto the benchmark HWC is plotted. In Figures 10-11 the P-wave field at the same two instants is projected onto the benchmark 2-helix fibre.

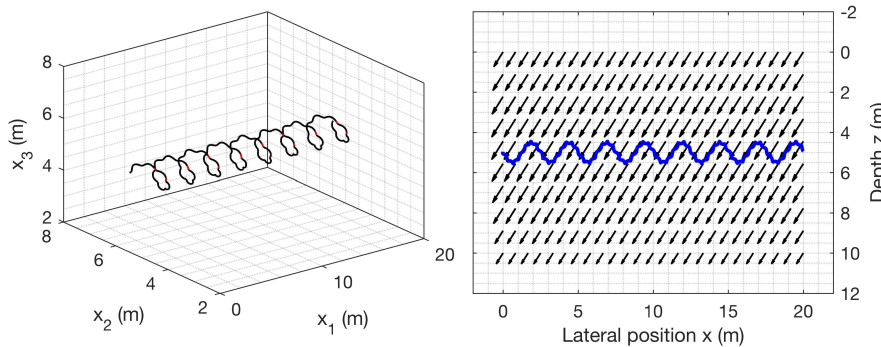


FIG. 10. Response of the benchmark 2-helix fibre (left panel) to a dynamic, plane-harmonic P-wave at oblique incidence (right panel). The displacement field at a given instant is plotted in the right panel, overlain by the projection of the fibre into the  $x_1$ - $x_3$  plane (blue). Intervals of the fibre in the right panel whose response exceeds a certain threshold are coloured red.

### Rayleigh-wave activation of shaped DAS fibres (dynamic)

We next exemplify the same benchmark fibres upon illumination by a plane-harmonic Rayleigh wave propagating in the  $x_1$  direction as developed in the previous section. The plotting configurations are the same

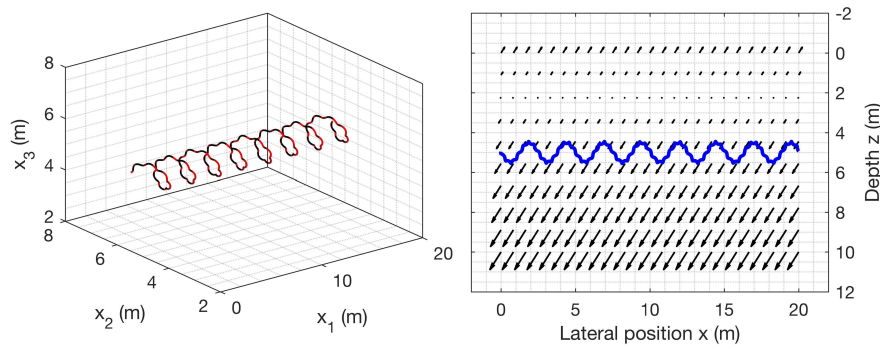


FIG. 11. Response of the benchmark 2-helix fibre (left panel) to a dynamic, plane-harmonic P-wave at oblique incidence (right panel). The displacement field at a given instant is plotted in the right panel, overlain by the projection of the fibre into the  $x_1$ - $x_3$  plane (blue). Intervals of the fibre in the right panel whose response exceeds a certain threshold are coloured red. This plot corresponds to the instant of time subsequent to that in Figure 10.

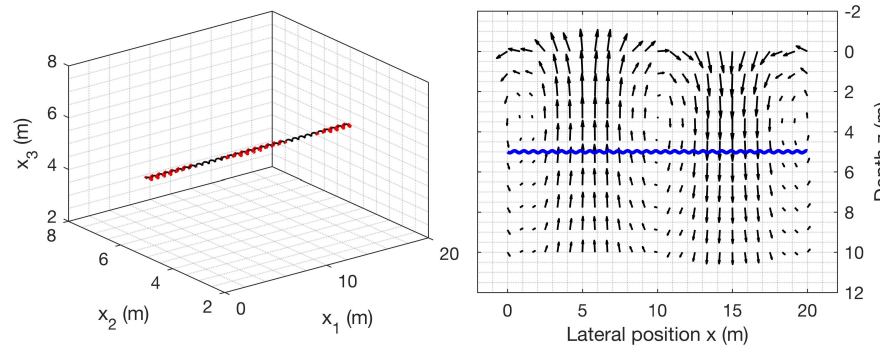


FIG. 12. Response of the benchmark HWC fibre (left panel) to a dynamic, plane-harmonic Rayleigh wave (right panel). The displacement field at a given instant is plotted in the right panel, overlain by the projection of the fibre into the  $x_1$ - $x_3$  plane (blue). Intervals of the fibre in the right panel whose response exceeds a certain threshold are coloured red.

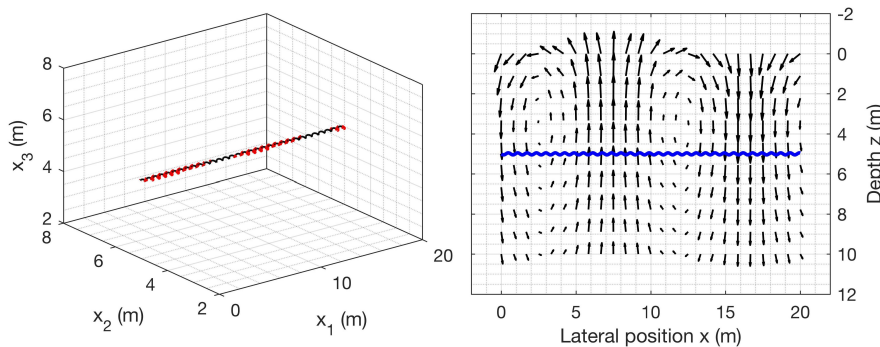


FIG. 13. Response of the benchmark HWC fibre (left panel) to a dynamic, plane-harmonic Rayleigh wave (right panel). The displacement field at a given instant is plotted in the right panel, overlain by the projection of the fibre into the  $x_1$ - $x_3$  plane (blue). Intervals of the fibre in the right panel whose response exceeds a certain threshold are coloured red. This plot corresponds to the instant of time subsequent to that in Figure 12.

*Effect of wavefield discretization*

A careful examination of the dynamic P-wave results in the surface wave examples reveals behaviour which may appear at odds with the behaviour seen in the static examples (e.g., Figure 4). In the top left panel of that Figure a vertically propagating P-wave is incident on a helical wound fibre. If the response were rotated such that the observer were looking down the  $x_1$  axis, such that we were looking through the helix as if it were a telescope, we would see, more or less as expected, that the regions of *insensitivity* were at the top and bottom arcs of the helix — where the P-wave was largely broadside.

In contrast, in Figure 13, even when the displacement is largely similar to the displacement of an upgoing P-wave (e.g., between 5-10m laterally) we tend not to see responses characterized by insensitivity at the top and bottom of the helix. Rather, looking at where the fibre in the left panel is red, we seem to instead see periodicity spanning many helix rotations.

The difference between the responses seen in Figures 4 and 13 is controlled by the discretization used in the wavefield that is input to the model in order to determine the response. If the wavefield is much more coarsely-sampled than is the fibre, as it is in the dynamic cases, the response will show the influence of both of these sampling rates. When using the FGSM coupled to a wave simulation in order to analyze the response or generate synthetics, choosing (i) computationally tractable but (ii) mutually supportive discretizations is important.

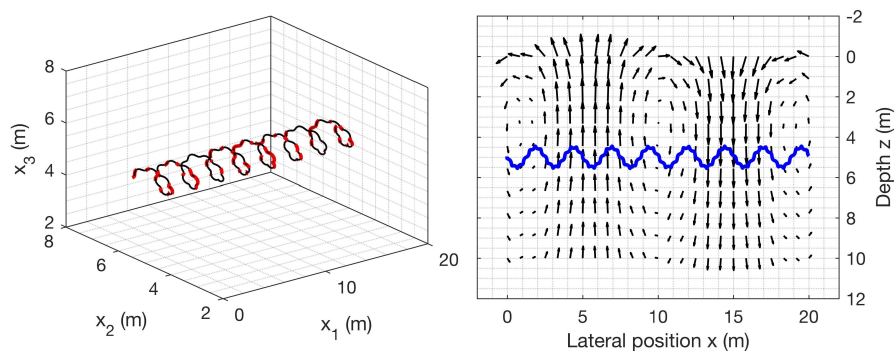


FIG. 14. Response of the benchmark 2-helix fibre (left panel) to a dynamic, plane-harmonic Rayleigh wave (right panel). The displacement field at a given instant is plotted in the right panel, overlain by the projection of the fibre into the  $x_1$ - $x_3$  plane (blue). Intervals of the fibre in the right panel whose response exceeds a certain threshold are coloured red.

**FIBRE DESIGN CRITERIA**

In Figure 1, the basic flow of the FGSM is laid out. Fibre shape parameters (e.g., radii and turning rates of all orders of helix), which we will contain in the vector  $\Lambda_n$  and other constraints such as gauge length ( $\gamma$ ) and channel separation ( $\zeta$ ) all contribute to determining the response of the fibre  $e_{tt}(s, t)$  at all points  $s$  along its arc-length and at all times  $t$ .

The orange path in the flowchart can be understood as an operator  $\mathcal{F}$  which takes an input strain field, a 6C tensor  $e(\mathbf{x}, t)$  varying with time  $t$  and position  $\mathbf{x} = (x_1, x_2, x_3)^T$ ,

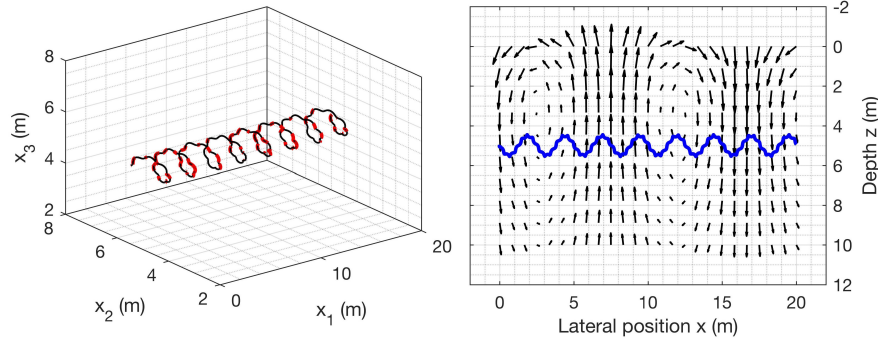


FIG. 15. Response of the benchmark HWC fibre (left panel) to a dynamic, plane-harmonic Rayleigh wave (right panel). The displacement field at a given instant is plotted in the right panel, overlain by the projection of the fibre into the  $x_1$ - $x_3$  plane (blue). Intervals of the fibre in the right panel whose response exceeds a certain threshold are coloured red. This plot corresponds to the instant of time subsequent to that in Figure 14.

and returns the fibre response:

$$e_{tt}(s, t) = \mathcal{F}(\gamma, \zeta, \Lambda_n) \mathbf{e}(\mathbf{x}, t). \quad (17)$$

In fact, given characteristic input strains from body waves,  $\mathbf{e}_P(\mathbf{x}, t)$  and  $\mathbf{e}_S(\mathbf{x}, t)$  we can determine characteristic fibre responses from those body waves. We can do the same with characteristic input strains from ground roll/Rayleigh wave energy,  $\mathbf{e}_R(\mathbf{x}, t)$ . And any other qualitatively or quantitatively discriminable type of wave. A list is generated:

$$\begin{aligned} e_{tt}^{P_i}(s, t_0) &= \mathcal{F}(\gamma, \zeta, \Lambda_n) \mathbf{e}_{P_i}(\mathbf{x}, t_0), \\ e_{tt}^{S_j}(s, t_0) &= \mathcal{F}(\gamma, \zeta, \Lambda_n) \mathbf{e}_{S_j}(\mathbf{x}, t_0), \\ e_{tt}^{R_k}(s, t_0) &= \mathcal{F}(\gamma, \zeta, \Lambda_n) \mathbf{e}_{R_k}(\mathbf{x}, t_0), \\ &\vdots \end{aligned} \quad (18)$$

in which  $i$ ,  $j$ , and  $k$  index various examples of these waves (e.g., as they vary with incidence angle, frequency, etc), and one or many instants of time  $t_0$  are incorporated. Suppose we also made the judgment call that certain of these modes (e.g., the body waves) were “good” and certain (e.g., surface waves) were “bad”, or simply that one set of these modes should be distinguished from another. Vectors of these values as  $s$  changes can be created:

$$\mathbf{d}_{P_i, t_0} = \begin{bmatrix} e_{tt}^{P_i}(s_0, t_0) \\ e_{tt}^{P_i}(s_1, t_0) \\ e_{tt}^{P_i}(s_2, t_0) \\ \vdots \end{bmatrix}, \quad (19)$$

and  $\mathbf{d}_{S_i, t_0}$ ,  $\mathbf{d}_{R_i, t_0}$ , etc., similarly. From these quantities a range of possible objective functions for fibre design are possible. For instance, if a Rayleigh wave and a P-wave tend to illuminate a particular fibre in a correlated manner, i.e., positions along the fibre which are strongly illuminated by a P-wave are also strongly illuminated by a Rayleigh wave, the scalar quantity

$$(\mathbf{d}_{P_i, t_0})^T (\mathbf{d}_{R_i, t_0}) \quad (20)$$

will tend to be large. Thus an objective function such as

$$\chi = \sum_{i,j,k,t_0} \left( (\mathbf{d}_{P_i,t_0})^T (\mathbf{d}_{R_i,t_0}) + \alpha (\mathbf{d}_{S_i,t_0})^T (\mathbf{d}_{R_i,t_0}) \right), \quad (21)$$

varied with respect to  $\Lambda_n$ , could be used to determine DAS-fibre shape parameters which produced responses for which the surface and body waves were minimally correlated, such that in processing separation was maximally straightforward. Or, an objective function penalizing Rayleigh waves

$$\chi' = \sum_{i,j,k,t_0} \left( (\mathbf{d}_{R_i,t_0})^T (\mathbf{d}_{R_i,t_0}) \right), \quad (22)$$

could also be varied to identify shapes which directly suppressed ground roll.

## CONCLUSIONS

One of the possible applications of the CREWES Fibre Geometry and Sensing Model is to allow for fibre shape design to be carried out. It remains to be seen what freedom fibre acquisition developers may have to lay out shapes of various types. Assuming some freedom will exist, we can model and appraise candidate shapes in advance, relative to their response to body and surface wave modes, or indeed to up- versus down-going waves, etc., and select designs which suppress, de-correlate, or accentuate one or the other mode. This is a work in progress.

## ACKNOWLEDGEMENTS

We thank the sponsors of CREWES for continued support. This work was funded by CREWES industrial sponsors and NSERC (Natural Science and Engineering Research Council of Canada) through the grant CRDPJ 461179-13.

## REFERENCES

- Ajo-Franklin, J., Lindsey, N., Dou, S., Daley, T. M., Freifeld, B., Martin, E. R., Robertson, M., Ulrich, C., and Wagner, A., 2015, A field test of Distributed Acoustic Sensing for ambient noise recording: SEG Expanded Abstracts.
- Anstey, N. A., 1986, Part 1: Whatever happened to ground roll?: The Leading Edge, **5**, No. 3, 40–45.
- Chalenski, D., Tatanova, M., Du, Y., Lopez, J., Mateeva, A., and Potters, H., 2016, Climbing the staircase of ultra-low cost 4D monitoring of deepwater fields using DAS-VSP: SEG Expanded Abstracts.
- Daley, T. M., Freifeld, B. M., Ajo-Franklin, J., Dou, S., Pevzner, R., Shulakova, V., Kashikar, S., Miller, D. E., Goetz, J., Hennings, J., and Lueth, S., 2013, Field testing of fiber-optic distributed acoustic sensing (DAS) for subsurface seismic monitoring: The Leading Edge, **32**, No. 6.
- Eaid, M., and Innanen, K. A., 2017, A coupled DAS shaped-fibre and 3D elastic finite difference wave model: CREWES Annual Report, **29**.
- Ewing, W. M., Jardetzky, W. S., and Press, F., 1957, Elastic waves in layered media: McGraw-Hill Book Co.
- Innanen, K. A., 2016, A geometrical model of DAS fibre response: CREWES Annual Report, **28**.

- Innanen, K. A., 2017, Determination of seismic tensor strain from HWC-DAS cable with arbitrary and nested-helix winds: SEG Expanded Abstracts.
- Innanen, K. A., and Mahmoudian, F., 2017, Towards optimal detection and characterization of microseismic sources with shaped DAS fibre: CREWES Annual Report, **29**.
- Kuvshinov, B. N., 2016, Interaction of helically wound fibre-optic cables with plane seismic waves: Geophysical Prospecting, **64**, 671–688.
- Lawton, D. L., 2017, DAS and seismic installations at the CaMI Field Research Station: CREWES Annual Report, **29**.
- Mateeva, A., Lopez, J., Mestayer, J., Wills, P., Cox, B., Kiyashchenko, D., Yang, Z., Berlang, W., Detomo, R., and Grandi, S., 2013, Distributed Acoustic Sensing (DAS) for reservoir monitoring with VSP: The Leading Edge, **32**, 1278–1283.
- Mateeva, A., Lopez, J., Potters, H., Mestayer, J., Cox, B., Kiyashchenko, D., Wills, P., Grandi, S., Hornman, K., Kuvshinov, B., Berlang, W., Yang, Z., and Detomo, R., 2014, Distributed acoustic sensing for reservoir monitoring with vertical seismic profiling: Geophysical Prospecting, **62**, 679–692.
- Mateeva, A., Mestayer, J., Cox, B., Kiyashchenko, D., Wills, P., Lopez, J., Grandi, S., Hornman, K., Lumens, P., Franzen, A., Hill, D., and Roy, J., 2012, Advances in Distributed Acoustic Sensing (DAS) for VSP: SEG Expanded Abstracts.
- Ning, I. L. C., and Sava, P., 2016, Multicomponent Distributed Acoustic Sensing: SEG Expanded Abstracts.